Journal of
Materials Chemistry A

ROYAL SOCIETY
OF CHEMISTRY

PAPER

View Article Online
View Journal | View Issue

Check for updates

Cite this: *J. Mater. Chem. A*, 2022, **10**, 20071

Laser synthesis of amorphous CoS_x nanospheres for efficient hydrogen evolution and nitrogen reduction reactions†

Lili Zhao,‡[a] Bin Chang, ‡[ad] Tianjiao Dong,‡[a] Haifeng Yuan,[a] Yue Li,[a] Zhenfei Tang,[a] Zhen Liu,[a] Hong Liu, [ab] Xiaoli Zhang [c] and Weijia Zhou *[a]

Transition metal sulfides (TMSs) have been demonstrated to be excellent electrode materials for various applications of electrochemical energy conversion and storage. However, the synthesis of TMSs through conventional approaches commonly suffers from toxic or environmentally unfriendly reagents as well as time consuming procedures, high thermal power and energy loss. Herein, CoS_x nanospheres with uniform distribution and strong adhesion on carbon fiber cloths (CoS_x/CC-L) are synthesized *via* the confined laser temperature field under a H_2S atmosphere under normal temperature and pressure conditions. It is demonstrated that the high pressure field induced by a laser yields amorphous CoS_x containing numerous S vacancies, which could provide more active sites for enhancing the hydrogen evolution reaction (HER) and nitrogen reduction reaction (NRR). The as-prepared CoS_x/CC-L exhibits a low overpotential of ~87 mV at 10 mA cm^{-2} for the HER in 0.5 M H_2SO_4 aqueous electrolyte and maintains a stable catalytic performance for 15 h with a high current density of 650 mA cm^{-2}. In addition, a high ammonia (NH_3) production rate (12.2 μg h^{-1} cm$_{cat}^{-2}$) and Faraday efficiency (10.1%) of CoS_x/CC-L at −0.2 V *vs.* RHE in a neutral 0.05 M Na_2SO_4 electrolyte were obtained. The good proton activation and nitrogen adsorption abilities arising from the sulfur vacancies contribute to the active nitrogen association/hydrogenation process during the NRR. The laser synthesis provides an alternative process to produce efficient amorphous catalysts, which are expected to be promising HER and NRR electrocatalysts for energy conversion applications.

Received 13th March 2022
Accepted 8th July 2022

DOI: 10.1039/d2ta01982e

rsc.li/materials-a

---

[a] *Institute for Advanced Interdisciplinary Research (iAIR), School of Chemistry and Chemical Engineering, University of Jinan, Jinan, 250022, P. R. China. E-mail: ifc_zhouwj@ujn.edu.cn*

[b] *State Key Laboratory of Crystal Materials, Shandong University, Jinan, 250100, P. R. China*

[c] *School of Materials Science and Engineering, Zhengzhou University, Zhengzhou, 450001, P. R. China*

[d] *State Key Laboratory of Photocatalysis on Energy and Environment, Fuzhou University, Fuzhou, 350116, P. R. China*

† Electronic supplementary information (ESI) available. See https://doi.org/10.1039/d2ta01982e

‡ These authors contributed equally to this work.

Prof. Weijia Zhou completed his PhD at Shandong University in 2012. Now, Dr Zhou is a professor at the Institute for Advanced Interdisciplinary Research (iAIR), University of Jinan, Shandong. His research interests are related to the design and synthesis of functional materials and devices for clean energy conversion and circulation, including photo and electro-catalytic water splitting and CO_2 reduction. More than 100 representative papers in Energy Environ. Sci., Angew. Chem., Int. Ed., ACS Nano, etc. were published, including one of the 100 most influential international academic papers in China and 12 ESI highly cited papers. He was awarded "Global Highly Cited Scientist" in 2018.

Introduction

The production of renewable hydrogen (H_2) fuel from water splitting and NH_3 from the nitrogen reduction reaction is attractive as a promising and vibrant strategy for green energy storage.[1,2] The HER for electrochemical water splitting and the NRR for electrochemical nitrogen fixation are of great significance, which are highly dependent on electrocatalytic materials with excellent catalytic activity.[3–5] Currently, precious metals are the most excellent electrocatalysts for electrochemical ammonia and hydrogen production, especially palladium-based nanomaterials for the NRR[6] and platinum-based nanomaterials for the HER[7] due to their moderate electronic structure to adsorb intermediates. However, the high cost and insufficient reserves of precious metals have severely restricted their practical applications. The development of low-cost, earth-abundant and non-precious electrocatalysts is significant for achieving large-scale hydrogen and ammonia production. TMSs have been widely employed as non-precious electrocatalysts for efficient water splitting and nitrogen reduction reactions. In the past decade, a variety of approaches have been performed for the synthesis of TMSs, including the hydrothermal method,[8] the coprecipitation method,[9] the sol–gel method[10] and the high-temperature calcination process.[11] Nevertheless, the strategies through these conventional approaches commonly suffer from toxic or environmentally unfriendly reagents and some issues of high thermal power, long synthesis time and energy loss. Thus, new technologies for large-scale production of TMSs with specific structures are necessary.

As an alternative candidate, laser synthesis has been reported to produce diverse nanomaterials with advantages of being cost-effective, time-saving, non-contact, maskless and environmentally friendly. The laser processing for material synthesis is realized by the photothermal reaction through an irradiated laser generating a confined temperature field at the desired position. Tour *et al.*[12] used a laser direct-write process to fabricate the HER and oxygen evolution reaction (OER) electrocatalytic electrodes on opposite faces of a commercial polyimide (PI) sheet for overall water splitting, where the impregnation of a PI film in a Pt ion solution and subsequent laser-induced graphene (LIG) forming process were utilized and efficient HER and OER activities were demonstrated. It was noteworthy that these strategies for laser synthesis of electrocatalysts were primarily performed to obtain oxides,[13] carbides[14] and LIG-based materials.[15,16] For laser-induced TMSs, laser synthesis in liquid was the most common method.[17,18] For instance, through nanosecond pulsed laser processing of an aqueous precursor solution, nickel sulfide with excellent electrocatalytic HER activity (-159 mV *vs.* RHE at 10 A g^{-1}) and long-term durability were achieved.[19] However, the TMSs synthesized by this method were primarily in powder-like form and the three-dimensional electrode with a large size was difficult to achieve. Therefore, how to expand the variety of catalysts and fabricate three-dimensional electrodes without a binder by laser synthesis will take more effort.

In this work, we demonstrated a facile approach toward the fabrication of CoS_x nanospheres anchored on carbon fiber cloths (CoS_x/CC-L) by using laser ablation of a Co-MOF grown on carbon fiber cloths (Co-MOF/CC) under a H_2S atmosphere. Herein, H_2S as the gas sulfur source reacted with Co-MOF/CC under the confined temperature field generated by a laser, which was a safe and green method without high temperature and high pressure. In particular, the CoS_x/CC-L with a large size of 10 cm × 10 cm was prepared within a short time of 16 min, which was directly used as a multifunctional electrode for the HER in acidic electrolyte and NRR in neutral electrolyte. As the HER electrode, CoS_x/CC-L exhibited a low overpotential ($\sim$87 mV at 10 mA cm^{-2}) in 0.5 M H_2SO_4 aqueous electrolyte. Meanwhile, owing to its excellent proton activation ability and amorphous structure, the CoS_x/CC-L sample also exhibited a high rate of NH_3 production of 12.2 μg h^{-1} cm_{cat}^{-2} and Faraday efficiency of 10.1% at -0.2 V *vs.* RHE for the NRR. The presence of S vacancies in amorphous CoS_x/CC-L due to the high pressure field induced by laser processing provided more active sites and then enhanced the HER and NRR activities.

Results and discussion

The schematic illustration of the fabrication process of CoS_x/CC-L is shown in Scheme 1. It was noteworthy that the as-prepared CoS_x/CC-L possessed good flexibility (Fig. S2†), and could be easily fabricated in a large scale, such as 10 cm × 10 cm (Fig. S3†) within 16 min, which was attributed to the time-saving advantage of the laser processing technique. The rapid processing and normal temperature conditions (Fig. S4†) were beneficial in reducing the emission of H_2S gas. The Co-MOF (ZIF-67) was first grown on the CC by immersing the CC into Co^{2+} and 2-methylimidazole mixed solution (Scheme 1a). As shown in Fig. 1a and S5,† the field emission scanning electron microscopy (SEM) images of Co-MOF/CC displayed uniform and compact Co-MOF nanosheets grown on the CC. X-ray diffraction (XRD) patterns confirmed the formation of ZIF-67 (ref. 20) (Fig. S6a†). In addition, the other peaks at approximately 25.3° and 43.3° corresponded to (002) and (100) facets of graphited carbon (JCPDS no. 41-1487). The laser synthesis of CoS_x/CC-L under a H_2S atmosphere was performed in a chamber with a light transmittable quartz window and valves for the inlet and outlet of gas (Scheme 1b). Before the laser irradiation, the chamber was bubbled with H_2S/Ar to remove the air. After pulsed laser irradiation, the sulfuration reaction between H_2S and the Co-MOF was carried out. Because of the high and confined power generated by the laser, the Co-

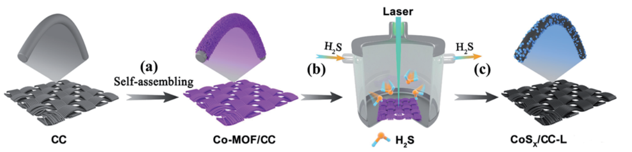

Scheme 1 Schematic illustration of the fabrication process of CoS_x/CC-L using a laser combined with a H_2S atmosphere (b and c) from Co-MOF/CC (a).

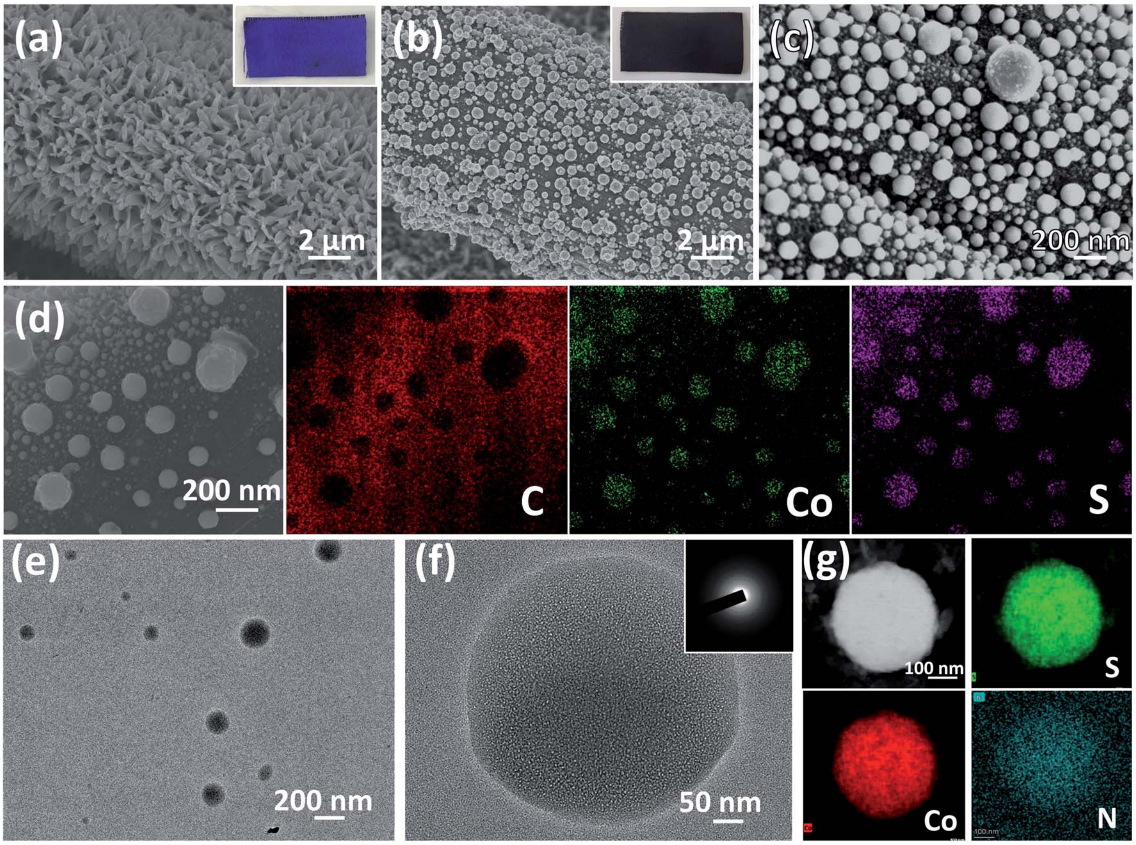

Fig. 1 SEM images of Co-MOF/CC (a) and CoS_x/CC-L (b and c). Insets are the corresponding photographs. (d) Corresponding EDS mapping of the C element, Co element and S element for CoS_x/CC-L. TEM (e) and HRTEM (f) images of CoS_x/CC-L. The inset in (f) is the SAED pattern of CoS_x/CC-L. (g) Elemental mapping of CoS_x nanospheres.

MOF sputtered and reacted with H_2S to be deposited onto the surface of CC (Scheme 1c). As observed in the SEM images shown in Fig. 1b and c, the CoS_x nanospheres with a diameter of 100–300 nm were evenly anchored on the surface of CC. Due to the decomposition of the Co-MOF grown on CC, a vast number of holes were formed on the surface of the CC (Fig. S7†), which was favorable for the anchoring of CoS_x nanospheres on CC with strong adhesion. The energy dispersive X-ray spectroscopy (EDS) mapping results revealed that a large number of CoS_x nanospheres are anchored on the surface of CC and the uniform distribution of Co and S elements of CoS_x nanospheres can be clearly identified (Fig. 1d). A low EDS signal for the N element was also detected (Fig. S6b and S8†). However, the corresponding XRD pattern for CoS_x/CC-L did not exhibit apparent diffraction peaks of CoS_2, except for those of the carbon substrate and MOF-derived $C_{11}H_{10}$ (Fig. S6a†), verifying the formation of amorphous CoS_x. Additionally, the transmission electron microscopy (TEM) images (Fig. 1e and f) showed that no lattice fringes were observed, and a typical halo around the bright spot in the center of amorphous materials was detected from the selected area electron diffraction pattern (SAED) (inset of Fig. 1f). These results further demonstrated that the as-obtained CoS_x possessed an amorphous nature. The elemental mapping results (Fig. 1g) showed that the S and Co elements were uniformly distributed in a single CoS_x nanosphere and the molar ratio of Co : S was about 1 : 1.15, which was obtained from the EDS results during TEM measurement and was determined according to the spectral peak area and correction factor. The relatively weak N element signal was also detected in the whole region including CoS_x nanospheres and the surrounding carbon fiber, implying that N-doped carbon and N-doped CoS_x were formed, consistent with the XPS results (Fig. S9c†).

In order to further confirm the chemical composition of the as-prepared CoS_x/CC-L, Raman spectra and X-ray photoelectron spectroscopy (XPS) spectra were evaluated. Raman spectra of CoS_x/CC-L (Fig. 2a) showed that the peaks located at 188.9, 467.7, 507.2, and 678.9 cm^{-1} could be assigned to the characteristic peaks of CoS_x.[21,22] Two additional peaks appearing at 1335 cm^{-1} and 1590 cm^{-1} could be indexed to defective carbon (D band) and sp^2-graphitic carbon (G band), respectively. Thus, the above results could verify the formation of CoS_x from the Co-MOF on CC. As depicted by the survey XPS spectra in Fig. S9a,† Co, S, C, N and O were detected in CoS_x/CC-L and CoS_2/CC. For the Co-MOF/CC, no S element appeared. Fig. 2b shows the high-resolution Co 2p spectra of the three samples. The Co 2p spectrum of Co-MOF/CC is composed of only Co^{2+} $2p_{3/2}$ and $2p_{1/2}$ at 781.1 eV and 796.6 eV, respectively, and the corresponding satellite peaks. For CoS_x/CC-L, three strong peaks were deconvoluted for each Co $2p_{3/2}$ and Co $2p_{1/2}$: the peaks centered at

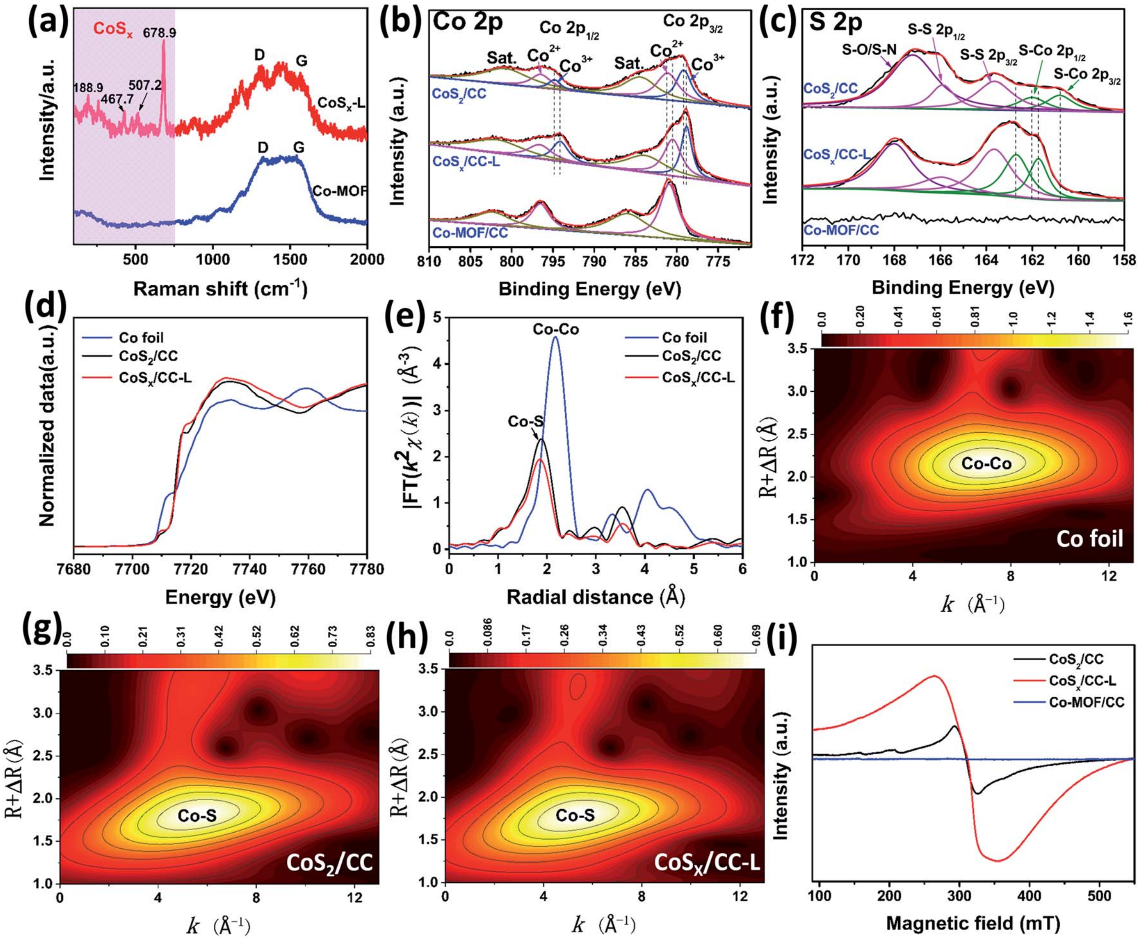

Fig. 2 (a) Raman spectra and high-resolution XPS spectra of the Co 2p (b), S 2p (c) for Co-MOF/CC, CoS_x/CC-L and CoS_2/CC. (d) Normalized Co K-edge XANES spectra and (e) Fourier transform of k^2-weighted Co EXAFS spectra of Co foil, CoS_x/CC-L and CoS_2/CC. (f–h) WT-EXAFS spectra of the Co foil, CoS_2/CC and CoS_x/CC-L. (i) EPR spectra of Co-MOF/CC, CoS_x/CC-L and CoS_2/CC.

778.8 and 794.2 eV were ascribed to Co^{3+} and those at 780.7 and 796.6 eV to Co^{2+}, while the corresponding satellite peaks appeared at 784.1 and 801.9 eV. The results suggested that mixed Co^{2+} and Co^{3+} oxidation states were formed in CoS_x/CC-L.[23,24] With regard to the S 2p high-resolution spectrum of CoS_x/CC-L (Fig. 2c), the characteristic peaks at 161.7 eV, 162.7 eV, 163.6 eV, 166.2 eV, and 168.0 eV are attributed to S–Co $2p_{3/2}$, S–Co $2p_{1/2}$, S–S $2p_{3/2}$, S–S $2p_{1/2}$ and S–O/S–N bonding,[25,26] respectively. The coexistence of Co and S elements confirmed the formation of CoS_x in the CoS_x/CC-L sample.

For comparison, crystallographic cobalt sulfide on CC was synthesized by calcination of Co-MOF/CC under a H_2S atmosphere at 600 °C, and the corresponding XRD pattern and SEM images of the as-obtained CoS_2/CC are shown in Fig. S10 and **S11**.† The as-obtained CoS_2/CC showed well-defined peaks corresponding to (111), (200), (210), (211), (220), (311), (222), (023) and (321) planes of CoS_2 (PDF 70-2865), which demonstrated that crystalline cobalt sulfide was obtained (Fig. S10†). In addition, the SEM image in Fig. S11† showed that the obtained CoS_2 on CC had irregular morphology, which also confirmed the advantage of laser synthesis. Furthermore, the XPS results (Fig. 2b, c and S9†) revealed a negative shift of Co 2p and positive shift of S–Co for CoS_x/CC-L compared with CoS_2/CC, which verified the higher density of Co electronic states in CoS_x/CC-L. This suggested that there were more S vacancies in CoS_x/CC-L due to the high pressure field induced by laser processing, which was consistent with the XRD result (Fig. S6a and S10†). The high-resolution spectrum of C 1s for CoS_x/CC-L could be divided into four peaks after peak de-convolution (Fig. S9b†), corresponding to C═O, C–S/C–N, C–C/C═C and C–Co bonding at 287.1 eV, 285.4 eV, 284.5 eV and 281.9 eV,[26] respectively. This result suggested that CoS_x nanospheres anchored on the surface of CC with a strong bonding interaction, which was beneficial to the fast electron transfer from CC to CoS_x nanospheres. The high-resolution spectrum of N 1s for CoS_x/CC-L could be divided into two main peaks corresponding to the pyridinic and graphitic nitrogen (Fig. S9c†). Combined with the EDS results for the N element, it was confirmed that nitrogen mainly existed in the form of a small amount of dopant. The high-resolution spectrum of O 1s for CoS_x/CC-L showed that the lattice oxygen (O_L) peak at 529.6 eV attributed to O–Co and adsorbed oxygen (O_{Ad}) peak at 531.2 eV attributed to the absorbed oxygen at the S vacancy site were observed, which came from surface oxidation of CoS_x. The laser preparation process resulted in less surface oxidation of CoS_x compared with that of CoS_2 (Fig. S9d†).

For further gaining more accurate structural information about the coordination environments of cobalt atoms in CoS_x/CC-L, X-ray absorption near edge structure (XANES) and extended X-ray absorption fine structure (EXAFS) spectroscopy were performed for CoS_x/CC-L, CoS_2/CC and Co foil. As shown in Fig. 2d, the Co K-edge XANES spectrum of CoS_x/CC-L exhibited a 1s → 3d pre-edge peak at 7710.1 eV. Additionally, the highly similar spectrum variation of the Co K-edge XANES of CoS_x/CC-L and CoS_2/CC indicated that they possessed a similar cobalt coordination environment. The Co EXAFS data was further checked to achieve the quantitative information about bond lengths, coordination numbers and structural disorder. As shown in Fig. 2e, the Fourier transform (FT) of the k^2-weighted Co EXAFS spectrum of CoS_x/CC-L gave the Co–S coordination information while no Co–Co coordination was detected. Furthermore, the Co K-edge WT-EXAFS of these three samples (Fig. 2f–h) showed that the peak signal for CoS_x/CC-L was highly similar to that for CoS_2/CC, indicating the existence of a Co–S signal in CoS_x/CC-L. The Co–S distance at 1.86 Å (without phase correction) was resolved from the FT analysis. It was noteworthy that the fitting coordination number of Co–S in CoS_x/CC-L was slightly lower than that in CoS_2/CC (Table S1†), possibly because of the amorphous nature of CoS_x in CoS_x/CC-L that creates numerous S vacancies from laser processing. These above results further demonstrated the formation of amorphous CoS_x.

Since the elemental mapping of CoS_x nanoparticles in Fig. 1g implied the molar ratio of Co : S was about 1 : 1.15, the sulfur vacancies should be present. Therefore, the electron paramagnetic resonance (EPR) spectra of Co-MOF/CC, CoS_x/CC-L and CoS_2/CC were applied to verify the existence of S vacancies in CoS_x/CC-L. As shown in Fig. 2i, CoS_x/CC-L exhibited the EPR signals at $g = 2.001$, which was attributed to the trapped electrons from the S vacancies.[27] The Co-MOF/CC sample exhibited a very low signal at the same position, demonstrating that S vacancies have been formed in CoS_x/CC-L. In addition, the CoS_x/CC-L presented a much stronger EPR signal than CoS_2/CC, confirming the existence of more sulfur vacancies in CoS_x/CC-L, induced by the high pressure field during laser processing, which could provide more active sites and thus enhance the HER and NRR activities.[28]

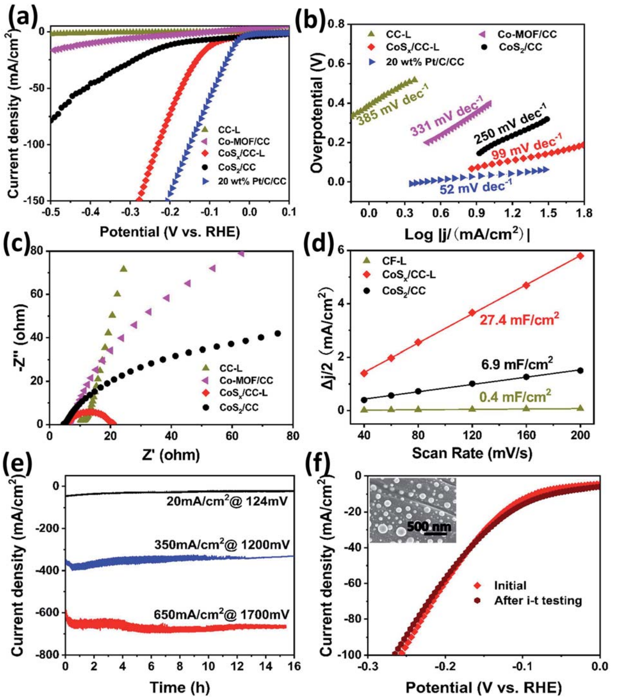

Fig. 3 (a) Polarization curves of CoS_x/CC-L and control samples in 0.5 M H_2SO_4. (b) Corresponding Tafel plots derived from (a). (c) Nyquist plots at an overpotential of 200 mV, and (d) the capacitive currents as a function of scan rates for CoS_x/CC-L and control samples. (e) Current–time plots with different overpotentials of 124 mV, 1200 mV and 1700 mV. (f) HER polarization curves of CoS_x/CC-L before and after *i*–*t* testing at 1200 mV. The inset is the SEM image of CoS_x/CC-L after *i*–*t* testing.

The HER performance of the CoS_x/CC-L and control samples of CC-L (SEM image in Fig. S12†), Co-MOF/CC and CoS_2/CC, was measured in a standard three-electrode configuration with IR-compensation to exclude the influence of the series resistance (R_s) arising from the solution, electrochemical workstation and electrodes in 0.5 M H_2SO_4 aqueous electrolyte. As shown in Fig. 3a, the CC processed by the laser under a H_2S atmosphere (CC-L) displayed almost no HER performance. CoS_x/CC-L (with an overpotential of ∼87 mV at 10 mA cm^{-2}) exhibited a much better HER performance than CC-L and Co-MOF/CC (∼396 mV at 10 mA cm^{-2}), indicating that the formed CoS_x nanospheres provided the active species for the HER. This could also be confirmed by the fact that H_2 bubbles were mainly generated on the area where the laser has processed (Video S1†). In addition, it is noteworthy that, although with the same composition phase as that of cobalt sulfide, the current density of CoS_x/CC-L was much higher than that of CoS_2/CC (with an overpotential of ∼178 mV at 10 mA cm^{-2}), implying that the abundant sulfur vacancies in CoS_x/CC-L were beneficial to enhance the HER performance, which is in agreement with the XPS and EPR spectra (Fig. 2). However, the overpotential value (∼87 mV) required to obtain a current density of 10 mA cm^{-2} was still poorer than that of commercial 20 wt% Pt/C (∼35 mV). For driving a current density of 100 mA cm^{-2}, CoS_x/CC-L and 20 wt% Pt/C required an overpotential of 229 mV and 150 mV, respectively. Through comparison with the other cobalt sulfide-based electrocatalysts, the HER activity of CoS_x/CC-L with a low overpotential of 87 mV to achieve −10 mA cm^{-2} in 0.5 M H_2SO_4 was better than or comparable to the leading cobalt sulfide-based HER catalysts, such as cobalt sulfide/reduced graphene oxide/carbon nanotubes (CoS_2/RGO–CNTs) (142 mV),[29] CoS_2 nanowires (145 mV),[30] $Co_{0.9}S_{0.58}P_{0.42}$ (139 mV),[31] surface selenized meso-CoS_2 (110 mV),[32] Co_9S_8@MoS_x (98 mV),[33] Co_9S_8-NDCL (96 mV),[34] Mo_2N/CoS_2 (85 mV),[35] $Zn_{0.30}Co_{2.70}S_4$ (80 mV),[36] CoS_2@MoS_2/RGO (98 mV),[37] Co_9S_8/MoS_2 (97 mV)[38] and Co_3S_4@MoS_2 (210 mV)[39] (Table S2†). For further studying the influence of N-doping on the achieved HER activity of CoS_x/CC-

L, we prepared control samples by laser processing Co-MOF/CC using the mixed gases of H_2S and NH_3 with their different ratios (10% NH_3/H_2S, 20% NH_3/H_2S and 50% NH_3/H_2S), to obtain different N doped CoS_x/CC-L samples (denoted as CoS_x/CC–10% NH_3-L, CoS_x/CC–20% NH_3-L and CoS_x/CC–50% NH_3-L). In addition, bare carbon cloth was processed using a laser under an NH_3 atmosphere to obtain the N-doped carbon cloth (CC–NH_3-L). The corresponding HER polarization curves of CC–NH_3-L, CoS_x/CC-L, CoS_x/CC–10% NH_3-L, CoS_x/CC–20% NH_3-L and CoS_x/CC–50% NH_3-L in 0.5 M H_2SO_4 are shown in Fig. S13.† The CC–NH_3-L displayed almost no HER activity, implying that the N-doped carbon did not contribute to the electrocatalytic performance in this work. Furthermore, CoS_x/CC-L exhibited a much better HER performance than CoS_x/CC–10% NH_3-L, CoS_x/CC–20% NH_3-L and CoS_x/CC–50% NH_3-L, suggesting that the increase in the nitrogen content decreased rather than enhancing the performance. This proves that the excellent HER activity of CoS_x/CC-L is solely attributed to the formed CoS_x spheres. The CoS_x/CC-L with different laser powers (6 W, 12 W and 18 W) were also synthesized, which were denoted as CoS_x/CC-L-6 W, CoS_x/CC-L-12 W and CoS_x/CC-L-18 W, respectively. As shown in Fig. S14,† the HER activity slightly increased with the increase of laser powers.

The Tafel slope revealed the inherent reaction dynamics of the HER (Fig. 3b). The iR-corrected Tafel slope value of 20 wt% Pt/C was 52 mV dec^{-1}. The corresponding Tafel slope value of 99 mV dec^{-1} for CoS_x/CC-L implied that the HER on CoS_x/CC-L proceeded through a Volmer–Heyrovsky mechanism and the electrochemical desorption process was the rate-limiting step. In addition, this Tafel slope was much smaller than those of CoS_2/CC (250 mV dec^{-1}), Co-MOF/CC (331 mV dec^{-1}) and CC-L (385 mV dec^{-1}), demonstrating a more efficient HER performance of CoS_x/CC-L. This is attributable to the laser-induced sulfur vacancies in CoS_x/CC-L, which facilitated the adsorption and reduction of H_3O^+ to form the H_{ads} intermediate, thus speeding up the Volmer reaction. Electrochemical impedance spectroscopy (EIS) was also performed and the Nyquist plots are shown in Fig. 3c and S15† to investigate the electrocatalytic kinetics of the HER. As is well known, the lower charge transfer resistance (R_{ct}) obtained from the semicircle in the low frequency zone corresponds to the faster reaction rate. As shown in Fig. 3c, the R_{ct} of CoS_x/CC-L was the smallest at an overpotential of 200 mV, indicating that CoS_x/CC-L had a faster electron transfer rate at the electrocatalyst/electrolyte interface and was more active. In addition, the decreased R_{ct} values of CoS_x/CC-L with progressive overpotentials from 100 mV to 200 mV in Fig. S15† also confirmed the advantageous HER kinetics towards the electrolyte interface. The double-layer capacitance (C_{dl}) was measured to evaluate the electrochemically active surface area (ECSA). As shown in Fig. 3d and S16,† the ECSA of CoS_x/CC-L (27.4 mF cm^{-2}) was much larger than those of CoS_2/CC (6.9 mF cm^{-2}) and CC-L (0.4 mF cm^{-2}), which was attributed to the high specific surface area of the formed CoS_x nanospheres and was beneficial to the exposure of more available active sites for the HER and diffusion of electrocatalytic active species.

For electrocatalytic HER, long-term catalytic stability is an important parameter for the possible practical application, especially at a large current density. Here, the catalytic durability of CoS_x/CC-L was assessed using current–time (*i*–*t*) plots (Fig. 3e) and polarization curves before and after *i*–*t* testing (Fig. 3f) in 0.5 M H_2SO_4 electrolyte. The negligible attenuations could be observed for continuous current–time plots at different overpotentials of *ca.* 124 mV, 1200 mV and 1700 mV with a current density of 20 mA cm^{-2}, 350 mA cm^{-2} and 650 mA cm^{-2}, respectively. With the almost identical polarization curves of CoS_x/CC-L before and after the *i*–*t* test (Fig. 3f) and no observed significant changes in the morphology (inset of Fig. 3f), as well as the remaining amorphous structure after HER measurements (Fig. S17†), the good long-term catalytic and structure stability for the HER could be verified.

The electrochemical reduction of N_2 to NH_3 provides an effective and sustainable strategy to store and carry hydrogen to produce on-demand fertilizers.[40] In addition, the synthesis of NH_3 is a process of active nitrogen association with active hydrogen, thus a certain proton activation ability is needed and this has been demonstrated in the HER performance for CoS_x/CC-L (Fig. 3). Considering that the enriched active hydrogen would directly result in hydrogen production under acidic conditions and thus reduce the selectivity of the NRR, we

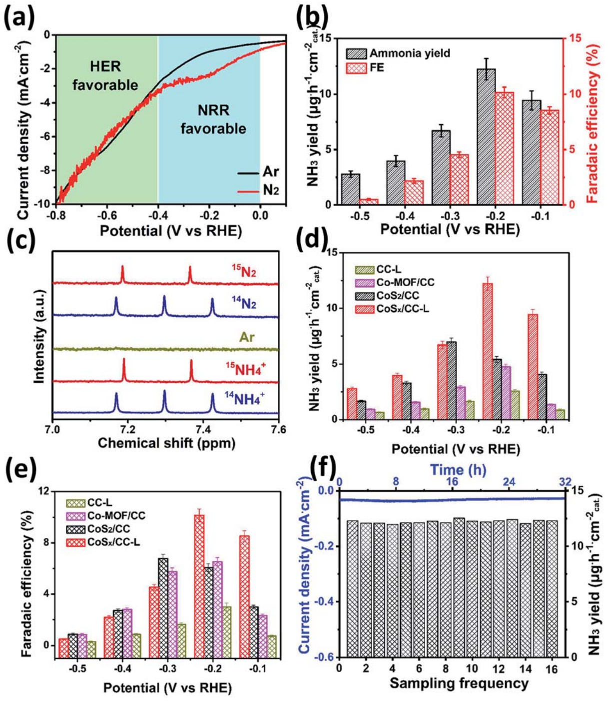

Fig. 4 (a) Polarization curves of CoS_x/CC-L under Ar and N_2 atmospheres. (b) Electrocatalytic NRR performance with NH_3 yield (black) and faradaic efficiency (red) for CoS_x/CC-L. (c) ^1H NMR analysis of the CoS_x/CC-L fed by $^{14}N_2$ and $^{15}N_2$ gases after electrochemical NRR process. Electrocatalytic NRR performances with NH_3 yield (d) and faradaic efficiency (e) for different samples at different overpotentials. (f) Chronoamperometry test results of CoS_x/CC-L for sixteen cycles (each for 2 h of electrolysis) at −0.2 V *vs.* RHE and the obtained NH_3 yields.

applied a lower cathodic overpotential and engineered the CoS_x/CC-L sample in a neutral electrolyte (0.05 M Na_2SO_4) to minimize the HER and increase the efficiency of the NRR. The best NH_3 yield and faradaic efficiency were achieved for the samples synthesized with a laser power of 18 W (Fig. S18†). Therefore we chose CoS_x/CC-L-18 W as the target sample. As shown by polarization curves (LSV) in Fig. 4a, the current density in a potential range of 0 V to −0.4 V *vs.* RHE of CoS_x/CC-L under a N_2 atmosphere was increased apparently in contrast to that under an Ar atmosphere, suggesting that this region was NRR favorable. When the polarization potential increased to be more negative than −0.4 V *vs.* RHE, the same current density for N_2 and Ar atmospheres demonstrated that this region was HER favorable. Then NRR characterization studies using CoS_x/CC-L as cathodic catalysts were performed under ambient conditions with continuous N_2 bubbling. After the corresponding *i*–*t* curves measurements at different potentials of −0.5 V to −0.1 V *vs.* RHE (Fig. S19†), the generated NH_3 was detected from the UV-vis absorption spectra by using the indophenol blue method (Fig. S20†), and the obtained NH_3 yields and FEs are displayed in Fig. 4b. As shown, the highest average NH_3 yield and the corresponding faradaic efficiency of CoS_x/CC-L were achieved at −0.2 V *vs.* RHE, reaching ∼12.2 $\mu g\ h^{-1}\ cm_{cat}^{-2}$ and 10.1%, respectively. At the more negative potentials, the NH_3 yields and FEs decreased gradually due to the competitive HER on the cathode.

The ^{15}N isotopic labeling experiment (Fig. 4c) was further used to confirm that the N source of NH_3 resulted from supplied N_2. The ^1H NMR spectra of commercial $^{14}NH_4Cl$ and $^{15}NH_4Cl$ samples were collected as standard spectra and the internal standard method and ^1H NMR spectra with different reactive times were utilized to verify the authenticity of the data (Fig. S21†). As shown, the ^1H NMR spectra for the electrolytes after NRR at −0.2 V showed a ^{14}N triple peak signal of $^{14}NH_4^+$ when using $^{14}N_2$ as the feeding gas. On the other hand, when using $^{15}N_2$ as the feeding gas, a ^{15}N doublet ($I = 1/2$) in the range of 7.2–7.4 ppm without obvious peaks of the ^{14}N triplet was detected. The peak positions for both the triplet and doublet closely matched the reference substances $^{14}NH_4Cl$ and $^{15}NH_4Cl$, demonstrating the successful production of ammonia during the NRR process and the detected NH_3 completely derived from the supplied N_2.

In order to demonstrate the effects of S vacancies on the NRR performance, the NRR performance analyses of CoS_x/CC-L and control samples CC-L, Co-MOF/CC and CoS_2/CC in neutral electrolyte at different potentials were carried out (Fig. S22†). As shown in Fig. 4d and e, the CoS_x/CC-L and CoS_2/CC possessed higher NH_3 yields and faradaic efficiency than Co-MOF/CC and CC-L, suggesting the vital role of CoS_x in catalytic NRR. In addition, compared with the optimal NH_3 yield and the faradaic efficiency (∼7.0 $\mu g\ h^{-1}\ cm_{cat}^{-2}$ and 6.8%) of CoS_2/CC at −0.3 V *vs.* RHE, the CoS_x/CC-L displayed higher electrocatalytic NRR activities of ∼12.2 $\mu g\ h^{-1}\ cm_{cat}^{-2}$ and 10.1% at a lower polarization potential of −0.2 V *vs.* RHE. This is most likely related to the S vacancies produced by laser processing, which could provide more adsorption sites for N_2. S vacancies as the electron-rich sites led to efficient N_2 adsorption by Co ions, which was beneficial for subsequent electrocatalytic N_2 activation.[41,42] For studying the influence of N-doping on the achieved NRR activity of CoS_x/CC-L, the NH_3 yields of CoS_x/CC-L, CoS_x/CC–10% NH_3-L, CoS_x/CC–20% NH_3-L and CoS_x/CC–50% NH_3-L were determined and compared (Fig. S23†). As shown, increasing the N-doping level did not enhance the NH_3 yields, and the optimal NRR performance was still 12.2 $\mu g\ h^{-1}\ cm_{cat}^{-2}$ for the CoS_x/CC-L sample at −0.2 V. As a consequence, the HER and NRR results for different N-doped samples indicated that N doping may affect the electrocatalytic performance, but HER and NRR activities were mainly derived from amorphous CoS_x in CoS_x/CC-L. For comparison, the performance of the CoS_x/CC-L was better than or comparable to most of the previously reported NRR catalysts[43–54] under neutral conditions, as illustrated in Table S3.† In addition, the synthesis of sulfide by a laser combined with a H_2S atmosphere is a universal method. The CuS_x/CC-L and FeS_x/CC-L were prepared by the laser processing of the Cu-MOF and Fe-MOF under a H_2S atmosphere and their NRR performance was measured (Fig. S24†). As shown, the optimal NH_3 yields for FeS_x/CC-L and CuS_x/CC-L were 15.5 $\mu g\ h^{-1}\ cm_{cat}^{-2}$ at −0.3 V *vs.* RHE and 13.6 $\mu g\ h^{-1}\ cm_{cat}^{-2}$ at −0.5 V *vs.* RHE, respectively. The excellent NNR activity demonstrated the advantages of laser processing as a universal method for the synthesis of amorphous sulfides.

The NRR stability of CoS_x/CC-L was evaluated using a chronoamperometry test at −0.2 V *vs.* RHE comprising sixteen cycles (each for 2 h of electrolysis) (Fig. 4f). As seen, no significant NH_3 yield attenuation occurred during the sixteen consecutive N_2 reduction cycles, verifying the excellent NRR catalytic stability for CoS_x/CC-L. No significant changes to the spherical morphology could be observed (Fig. S25†), confirming the structural integrity of CoS_x/CC-L. Meanwhile, the Faraday efficiency during the whole cycling process was calculated to be about 11.57%.

Conclusions

A facile approach toward the fabrication of amorphous CoS_x nanospheres anchored on carbon fiber cloths (CoS_x/CC-L) with uniform distribution and strong adhesion *via* the confined temperature field generated by a laser under a H_2S atmosphere was demonstrated, which was carried out within a short time and at normal temperature. The obtained CoS_x/CC-L was directly applied as an efficient and multifunctional electrode for electrocatalytic HER and electrocatalytic NRR. The amorphous nature of CoS_x nanospheres played a vital role in enhancing the HER and NRR activities. As a HER electrocatalyst, CoS_x/CC-L exhibited a low overpotential (∼87 mV at 10 mA cm^{-2}) in 0.5 M H_2SO_4 aqueous electrolyte. As a NRR electrocatalyst, the CoS_x/CC-L exhibited a high rate of NH_3 production of 12.2 $\mu g\ h^{-1}\ cm_{cat}^{-2}$ and Faraday efficiency of 10.1% at −0.2 V *vs.* RHE. The laser-produced amorphous CoS_x/CC-L catalyst was expected to be a promising HER and NRR electrocatalyst for large-scale application in energy conversion and storage fields.

Author contributions

Lili Zhao: data curation, formal analysis, investigation, writing the original draft, funding acquisition. Bin Chang:

methodology, supervision, validation. Tianjiao Dong: visualization, supervision, validation. Haifeng Yuan: formal analysis, supervision. Yue Li: software, validation. Zhenfei Tang: supervision, validation. Zhen Liu: supervision, validation. Hong Liu: project administration, resources, supervision, validation. Xiaoli Zhang: supervision, validation. Weijia Zhou: conceptualization, funding acquisition, project administration, resources, supervision, writing – review & editing.

Conflicts of interest

There are no conflicts to declare.

Acknowledgements

This work was supported by the Taishan Scholar Project of Shandong Province (tsqn201812083), the Natural Science Foundation of Shandong Province (ZR2019YQ20, ZR2019BB001, ZR2021JQ15, and ZR2021QE011), the Innovative Team Project of Jinan (2021GXRC019), the National Natural Science Foundation of China (51902132, 51972147, and 52022037), the China Postdoctoral Science Foundation (2021M701402), the Postdoctoral Innovative Talents Support Program of Shandong Province (SDBX2020009) and the Open Project Program of the State Key Laboratory of Photocatalysis on Energy and Environment (SKLPEE-KF202110).

Notes and references

1 H. Wu, H. N. Alshareef and T. Zhu, *InfoMat*, 2019, **1**(3), 417–425.

2 L. Du, L. Xing, G. Zhang, X. Liu, D. Rawach and S. Sun, *SusMat*, 2021, **1**(2), 150–173.

3 Q. Zhang and J. Guan, *Adv. Funct. Mater.*, 2020, **30**(31), 2000768.

4 P. Zhou, G. Zhai, X. Lv, Y. Liu, Z. Wang, P. Wang, Z. Zheng, H. Cheng, Y. Dai and B. Huang, *Appl. Catal., B*, 2021, **283**, 119590.

5 F. Yu, L. Wang, Q. Xing, D. Wang, X. Jiang, G. Li, A. Zheng, F. Ai and J.-P. Zou, *Chin. Chem. Lett.*, 2020, **31**(6), 1648–1653.

6 H. Liu, L. Syama, L. Zhang, C. Lee, C. Liu, Z. Dai and Q. Yan, *SusMat*, 2021, **1**(4), 482–505.

7 L. Zhang, K. Doyle-Davis and X. Sun, *Energy Environ. Sci.*, 2019, **12**(2), 492–517.

8 L. Zhao, J. Jia, Z. Yang, J. Yu, A. Wang, Y. Sang, W. Zhou and H. Liu, *Appl. Catal., B*, 2017, **210**, 290–296.

9 H.-F. Wang, C. Tang, B. Wang, B.-Q. Li and Q. Zhang, *Adv. Mater.*, 2017, **29**(35), 1702327.

10 T. Chen, Y. Ma, Q. Guo, M. Yang and H. Xia, *J. Mater. Chem. A*, 2017, **5**(7), 3179–3185.

11 L. Zhao, T. Dong, J. Du, H. Liu, H. Yuan, Y. Wang, J. Jia, H. Liu and W. Zhou, *Sol. RRL*, 2021, **5**(2), 2000415.

12 J. Zhang, C. Zhang, J. Sha, H. Fei, Y. Li and J. M. Tour, *ACS Appl. Mater. Interfaces*, 2017, **9**(32), 26840–26847.

13 G. Ou, P. Fan, H. Zhang, K. Huang, C. Yang, W. Yu, H. Wei, M. Zhong, H. Wu and Y. Li, *Nano Energy*, 2017, **35**, 207–214.

14 X. Zang, C. Shen, Y. Chu, B. Li, M. Wei, J. Zhong, M. Sanghadasa and L. Lin, *Adv. Mater.*, 2018, **30**(26), 1800062.

15 C. Thamaraiselvan, J. Wang, D. K. James, P. Narkhede, S. P. Singh, D. Jassby, J. M. Tour and C. J. Arnusch, *Mater. Today*, 2020, **34**, 115–131.

16 R. Ye, D. K. James and J. M. Tour, *Adv. Mater.*, 2019, **31**(1), 1803621.

17 A. M. Mostafa, E. A. Mwafy and M. S. Hasanin, *Opt. Laser Technol.*, 2020, **121**, 105824.

18 H. Zeng, X.-W. Du, S. C. Singh, S. A. Kulinich, S. Yang, J. He and W. Cai, *Adv. Funct. Mater.*, 2012, **22**(7), 1333–1353.

19 T.-F. Hung, Z.-W. Yin, S. B. Betzler, W. Zheng, J. Yang and H. Zheng, *Chem. Eng. J.*, 2019, **367**, 115–122.

20 Y. Pan, K. Sun, S. Liu, X. Cao, K. Wu, W.-C. Cheong, Z. Chen, Y. Wang, Y. Li, Y. Liu, D. Wang, Q. Peng, C. Chen and Y. Li, *J. Am. Chem. Soc.*, 2018, **140**(7), 2610–2618.

21 Q. Lu, J. Yu, X. Zou, K. Liao, P. Tan, W. Zhou, M. Ni and Z. Shao, *Adv. Funct. Mater.*, 2019, **29**(38), 1904481.

22 Y. Xiao, J.-Y. Hwang, I. Belharouak and Y.-K. Sun, *Nano Energy*, 2017, **32**, 320–328.

23 L. Yang, L. Zhang, G. Xu, X. Ma, W. Wang, H. Song and D. Jia, *ACS Sustainable Chem. Eng.*, 2018, **6**(10), 12961–12968.

24 T. Liu, P. Li, N. Yao, T. Kong, G. Cheng, S. Chen and W. Luo, *Adv. Mater.*, 2019, **31**(21), 1806672.

25 T. Yang, D. Yang, Y. Liu, J. Liu, Y. Chen, L. Bao, X. Lu, Q. Xiong, H. Qin, Z. Ji, C. D. Ling and R. Zheng, *Electrochim. Acta*, 2018, **290**, 193–202.

26 X. Liu, C. Hao, L. He, C. Yang, Y. Chen, C. Jiang and R. Yu, *Nano Res.*, 2018, **11**(8), 4169–4182.

27 L. Pan, S. Sun, Y. Chen, P. Wang, J. Wang, X. Zhang, J.-J. Zou and Z. L. Wang, *Adv. Energy Mater.*, 2020, **10**(15), 2000214.

28 B. Jin, X. Ye, H. Zhong, F. Jin and Y. H. Hu, *Chin. Chem. Lett.*, 2022, **33**(2), 812–816.

29 S. Peng, L. Li, X. Han, W. Sun, M. Srinivasan, S. G. Mhaisalkar, F. Cheng, Q. Yan, J. Chen and S. Ramakrishna, *Angew. Chem., Int. Ed.*, 2014, **53**(46), 12594–12599.

30 M. S. Faber, R. Dziedzic, M. A. Lukowski, N. S. Kaiser, Q. Ding and S. Jin, *J. Am. Chem. Soc.*, 2014, **136**(28), 10053–10061.

31 Z. Dai, H. Geng, J. Wang, Y. Luo, B. Li, Y. Zong, J. Yang, Y. Guo, Y. Zheng, X. Wang and Q. Yan, *ACS Nano*, 2017, **11**(11), 11031–11040.

32 B. Dutta, Y. Wu, J. Chen, J. Wang, J. He, M. Sharafeldin, P. Kerns, L. Jin, A. M. Dongare, J. Rusling and S. L. Suib, *ACS Catal.*, 2019, **9**(1), 456–465.

33 X. Zhou, X. Yang, M. N. Hedhili, H. Li, S. Min, J. Ming, K.-W. Huang, W. Zhang and L.-J. Li, *Nano Energy*, 2017, **32**, 470–478.

34 J. Mujtaba, L. He, H. Zhu, Z. Xiao, G. Huang, A. A. Solovev and Y. Mei, *ACS Appl. Nano Mater.*, 2021, **4**(2), 1776–1785.

35 Y. Zang, B. Yang, A. Li, C. Liao, G. Chen, M. Liu, X. Liu, R. Ma and N. Zhang, *ACS Appl. Mater. Interfaces*, 2021, **13**(35), 41573–41583.

36 Z.-F. Huang, J. Song, K. Li, M. Tahir, Y.-T. Wang, L. Pan, L. Wang, X. Zhang and J.-J. Zou, *J. Am. Chem. Soc.*, 2016, **138**(4), 1359–1365.

37 Y. Guo, L. Gan, C. Shang, E. Wang and J. Wang, *Adv. Funct. Mater.*, 2017, 1602699.

38 H. Zhu, G. Gao, M. Du, J. Zhou, K. Wang, W. Wu, X. Chen, Y. Li, P. Ma, W. Dong, F. Duan, M. Chen, G. Wu, J. Wu, H. Yang and S. Guo, *Adv. Mater.*, 2018, **30**, 1707301.

39 Y. Guo, J. Tang, H. Qian, Z. Wang and Y. Yamauchi, *Chem. Mater.*, 2017, **29**, 5566–5573.

40 N. C. Kani, A. Prajapati, B. A. Collins, J. D. Goodpaster and M. R. Singh, *ACS Catal.*, 2020, **10**(24), 14592–14603.

41 X. Zi, J. Wan, X. Yang, W. Tian, H. Zhang and Y. Wang, *Appl. Catal., B*, 2021, **286**, 119870.

42 X. Kong, H.-Q. Peng, S. Bu, Q. Gao, T. Jiao, J. Cheng, B. Liu, G. Hong, C.-S. Lee and W. Zhang, *J. Mater. Chem. A*, 2020, **8**(16), 7457–7473.

43 M. Arif, G. Yasin, L. Luo, W. Ye, M. A. Mushtaq, X. Fang, X. Xiang, S. Ji and D. Yan, *Appl. Catal., B*, 2020, **265**, 118559.

44 Y. Tian, B. Chang, G. Wang, L. Li, L. Gong, B. Wang, R. Yuan and W. Zhou, *J. Mater. Chem. A*, 2022, **10**(6), 2800–2806.

45 J. Zhou, X. Liu, X. Xu, X. Sun, D. Wu, H. Ma, X. Ren, Q. Wei and H. Ju, *ACS Sustainable Chem. Eng.*, 2021, **9**(40), 13399–13405.

46 B. Chang, L. Deng, S. Wang, D. Shi, Z. Ai, H. Jiang, Y. Shao, L. Zhang, J. Shen, Y. Wu and X. Hao, *J. Mater. Chem. A*, 2020, **8**(1), 91–96.

47 Y. Ma, T. Yang, H. Zou, W. Zang, Z. Kou, L. Mao, Y. Feng, L. Shen, S. J. Pennycook, L. Duan, X. Li and J. Wang, *Adv. Mater.*, 2020, **32**(33), 2002177.

48 Y. Guo, T. Wang, Q. Yang, X. Li, H. Li, Y. Wang, T. Jiao, Z. Huang, B. Dong, W. Zhang, J. Fan and C. Zhi, *ACS Nano*, 2020, **14**(7), 9089–9097.

49 N. Cao, Z. Chen, K. Zang, J. Xu, J. Zhong, J. Luo, X. Xu and G. Zheng, *Nat. Commun.*, 2019, **10**(1), 2877.

50 R. Zhang, J. Han, B. Zheng, X. Shi, A. M. Asiri and X. Sun, *Inorg. Chem. Front.*, 2019, **6**(2), 391–395.

51 R. Zhang, X. Ren, X. Shi, F. Xie, B. Zheng, X. Guo and X. Sun, *ACS Appl. Mater. Interfaces*, 2018, **10**(34), 28251–28255.

52 L. Zhang, X. Ji, X. Ren, Y. Ma, X. Shi, Z. Tian, A. M. Asiri, L. Chen, B. Tang and X. Sun, *Adv. Mater.*, 2018, **30**(28), 1800191.

53 X. Li, L. Li, X. Ren, D. Wu, Y. Zhang, H. Ma, X. Sun, B. Du, Q. Wei and B. Li, *Ind. Eng. Chem. Res.*, 2018, **57**(49), 16622–16627.

54 L. Zhang, X. Ren, Y. Luo, X. Shi, A. M. Asiri, T. Li and X. Sun, *Chem. Commun.*, 2018, **54**(92), 12966–12969.